

Full paper

Topological insulator nanoribbons – A new paradigm for high thermoelectric performance

Te-Hsien Wang^a, Horng-Tay Jeng^{a,b,c,*}^a Department of Physics, National Tsing Hua University, Hsinchu, 30013, Taiwan^b Physics Division, National Center for Theoretical Sciences, Hsinchu 30013, Taiwan^c Institute of Physics, Academia Sinica, Taipei, 11529, Taiwan

ARTICLE INFO

Keywords:

Thermoelectric
Boltzmann transport theory
Seebeck coefficient
Wiedemann-Franz law
Topological insulator
ZrTe₅

ABSTRACT

Thermoelectric (TE) materials, with the ability to convert heat directly to electricity, have attracted worldwide increasing attention due to the strong urge for clean energy today. However conventional TE devices suffer from the low conversion efficiency for decades due to the trade-off between TE parameters. Novel quantum materials such as topological insulators with unique boundary states protected topologically against backscattering offer a new way for designing high-performance TE devices. Here we demonstrate that topological insulator nanoribbons, which exhibit unconventional TE behaviors, can greatly improve the TE efficiency. As an example, we calculate the TE properties of the ZrTe₅ nanoribbon through the Boltzmann transport theory with the electronic bands and the thermal conductivity obtained from *ab initio* calculations. The dramatic difference in the scattering intensity between the in-gap topological edge states and the bulk states originates several unusual TE behaviors: (I) The electrical to electronic thermal conductivity ratio can be several times larger than that predicted by the Wiedemann-Franz law. (II) The reduced Seebeck coefficient shows an anomalous opposite sign to that of normal semiconductors with the magnitude much larger than unity. (III) By properly introducing defects, the thermal conductivity can be significantly reduced without noticeably deteriorating the electrical conductivity. (IV) Under appropriate strain, the electrical to electronic thermal conductivity ratio could be tens of times larger due to the bulk gap narrowing. These results indicate that a figure of merit larger than ten is highly likely.

1. Introduction

Nowadays the escalating energy crisis has become a global issue. It is imperative to find cleaner, more sustainable energy sources, and improve the efficiency of existing energy technologies. Among all the possible solutions, the thermoelectric (TE) generators, which can convert low graded heat into high quality electricity, having advantages of solid-state operation without moving parts, no release of greenhouse gases, good stability, and high reliability, have attracted widespread research interest [1–18]. Despite the vast potential impacts, the low energy conversion efficiency, difficult to compete with most traditional and commercial power generators, seriously restricts their applications [13,14].

The TE conversion efficiency of a given material is govern by the dimensionless figure of merit zT . To date, no material with $zT > 3$ has been reported [15,16]. The difficulty of searching for materials of high zT stems from the trade-off between the TE parameters. The figure of merit can be expressed as $zT = \sigma \tilde{S}^2 T / \kappa$, where T is the absolute

temperature, \tilde{S} the Seebeck coefficient, σ the electrical conductivity, and κ the thermal conductivity composed of the electronic part κ_e and the lattice part κ_L . It can also be expressed as $zT = CRS^2$ (Method section), in which $C \sim 0.3$ is a constant, $S = \tilde{S} / (k_B / e)$ the dimensionless reduced Seebeck coefficient, $R = \sigma / \kappa R_{WF}$ the ratio of the electrical conductivity σ to the thermal conductivity κ normalized by R_{WF} . Here, $R_{WF} = Ce^2 / k_B^2 T$ is the value of σ / κ expected from the Wiedemann-Franz (WF) law.

For metals, the electronic contribution κ_e is typically much larger than the lattice part κ_L so that the ratio R is approximately equal to $R_e = \sigma / \kappa_e R_{WF}$, which, according to the Wiedemann-Franz law, is nearly unity. As a result, the figure of merit is mostly determined by the magnitude of the reduced Seebeck coefficient, which is normally much smaller than unity, so that metals are in general not good TE materials with zT much smaller than unity. Insulators are commonly not good TE materials either because of their low electrical conductivity, even though they could have a large Seebeck coefficient. Typically, there is a trade-off between the electrical conductivity and the magnitude of the

* Corresponding author. Department of Physics, National Tsing Hua University, Hsinchu, 30013, Taiwan.

E-mail address: jeng@phys.nthu.edu.tw (H.-T. Jeng).<https://doi.org/10.1016/j.nanoen.2019.104092>

Received 21 June 2019; Received in revised form 20 August 2019; Accepted 2 September 2019

Available online 12 September 2019

2211-2855/ © 2019 The Authors. Published by Elsevier Ltd. This is an open access article under the CC BY-NC-ND license

<http://creativecommons.org/licenses/by-nc-nd/4.0/>.

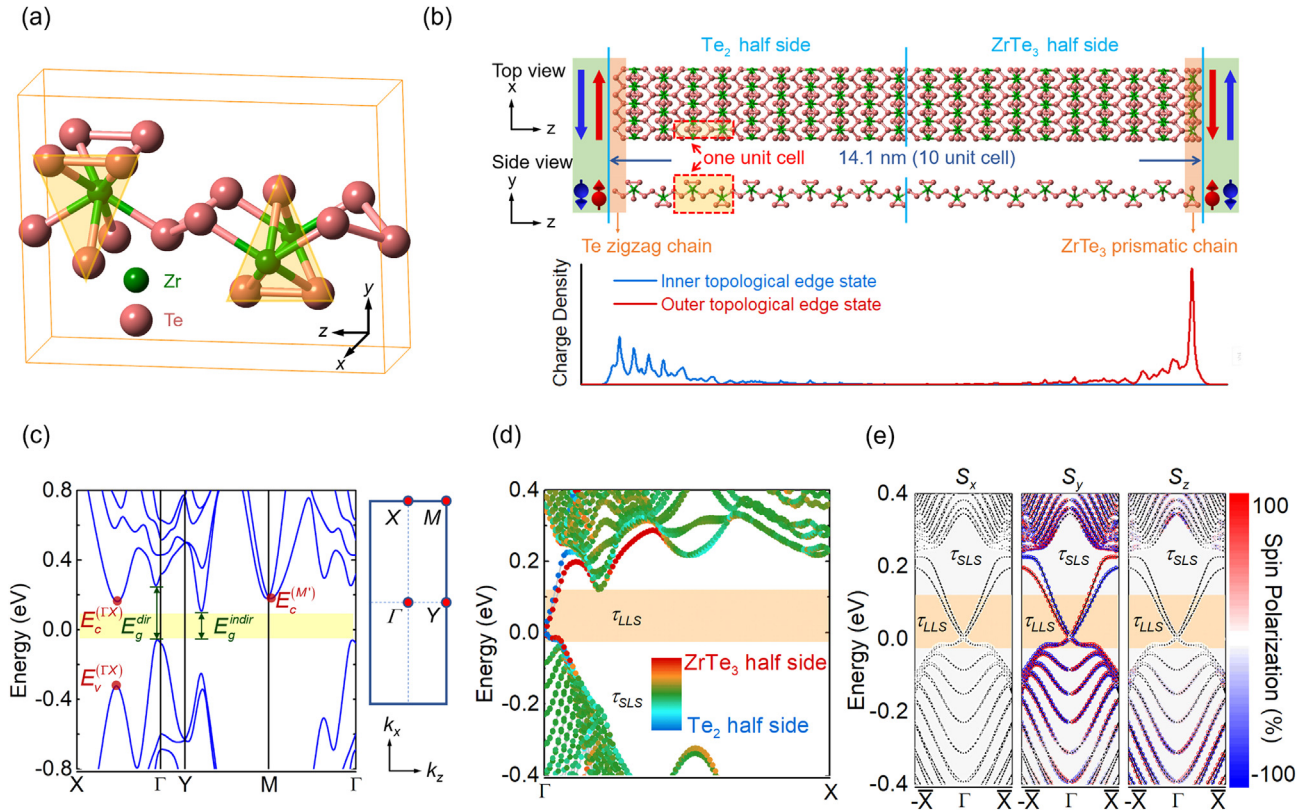


Fig. 1. Crystal structure, electronic bands, and spin texture of single-layer ZrTe₅ film and ribbon. (a) The single-layer film lies in the x - z plane. Its prismatic ZrTe₃ part is indicated by the shaded region. (b) Top view and side view of ZrTe₅ ribbon. The ribbon extends periodically along the x direction. Red-dashed rectangles indicate the monolayer unit cell. Different edge structures are composed of Te-zigzag chain (left) and ZrTe₃-prismatic chain (right) in the orange-shaded regions. The charge density profiles of the inner- and outer TESs show the decay lengths less than 3 nm with the electron distributions spatially separated from each other. The spin current at the ribbon edges are schematically illustrated beside the edges. (c) Electronic bands of single layer ZrTe₅. E_g^{dir} and E_g^{indir} indicate the direct and indirect gap, respectively. Strain effect can redefine the full gap E_g^{indir} by other band edges, $E_c^{(TX)}$, $E_v^{(TX)}$, or $E_c^{(M)}$. (d) Electronic bands of ZrTe₅ ribbon. The color of the dots represents the atomic contribution from the Te₂ (ZrTe₃) half side indicated in (b). The inner and outer linear TESs are clearly shown in the bulk band gap E_g^{Ribbon} (orange shaded region). (e) The spin-resolved electronic bands of the ZrTe₅ ribbon. The color of the circles indicates the x , y , z components of spin polarizations $\mathbf{S} = (S_x, S_y, S_z)$.

Seebeck coefficient: The electrical conductivity increases whereas the magnitude of the Seebeck coefficient decreases with increasing carrier concentration. Therefore, good TE materials are usually semiconductors with an optimized carrier concentration in between 10^{19} and 10^{21} carriers per cm^{-3} [3]. However, the ratio R is significantly smaller than unity in semiconductors because the lattice thermal conductivity κ_L is often much larger than the electronic counterpart κ_e . To enhance the ratio R and hence zT by reducing the κ_L , defects of different scales are usually introduced, but meanwhile, the electrical conductivity would be significantly impaired [1,15,19,20].

In mid 1990s, Dresselhaus et al. suggest that an extremely high $zT > 6$ ($zT > 14$) can be realized in 2D (1D) quantum systems [21,22]. Such enhancement of zT is mainly due to two reasons: an increase in density of states over a narrow energy range [23,24] and the strong phonon-boundary scattering in nanostructures. Their predictions have stimulated a new wave of interest in TE nanostructures [4,5,18]. Novel quantum materials such as topological insulators (TIs), which are insulating in their interior while exhibit unique topologically protected conducting boundary states on their surfaces or edges, offer a new way for designing high-performance TE devices [17,25]. The theoretically predicted intriguing spin-momentum locking effect of these topological surface (or edge) conduction electrons [26–28] have been experimentally [29–32] confirmed to be immune to the backscattering in the presence of non-magnetic impurities and defects. It has been observed in TI nanofilms that the topological surface states, with the relaxation time two orders of magnitude larger than the bulk one, can contribute

much higher electrical conductance in comparison with the bulk states [25,33,34]. Furthermore, the measured room-temperature power factor and figure of merit of TI thin films can be about ten times larger than the bulk counterparts [35,36]. The dramatic difference in the relaxation times between the two electronic transport channels of different dimensionality in TI nanostructures, as will be discussed, will lead to unconventional TE behaviors and hence unprecedented high figure of merit.

In this article, we demonstrate for single-layer topological insulator ZrTe₅ [37–39] nanoribbons, the dramatic difference in the relaxation time between the backscattering-free in-gap topological edge states (TESs) and the highly scattering 2D bulk states gives rise to several unusual TE behaviors greatly improving the TE efficiency. **(I) Anomalous Seebeck effect:** The magnitude of the reduced Seebeck coefficient in TI nanoribbons is much larger than unity with an opposite sign to its bulk counterpart. The anomalous sign of the Seebeck coefficient was theoretically predicted [40] and then experimentally observed in $(\text{Bi}_{1-x}\text{Sb}_x)_2\text{Te}_3$ thin films [41]. **(II) Wiedemann-Franz law violation:** The ratio of the electrical conductivity to the electronic thermal conductivity can be several times larger than that given by the Wiedemann-Franz law, which was thought as a quite robust law for conventional materials. The violation of Wiedemann-Franz law in TI nanostructures was theoretically predicted very recently [25]. Since (II) is based on the same assumption of relaxation times as (I), the observation of the anomalous sign of the Seebeck coefficient in Ref. [41] can be taken as an indirect evidence that the Wiedemann-Franz law is substantially

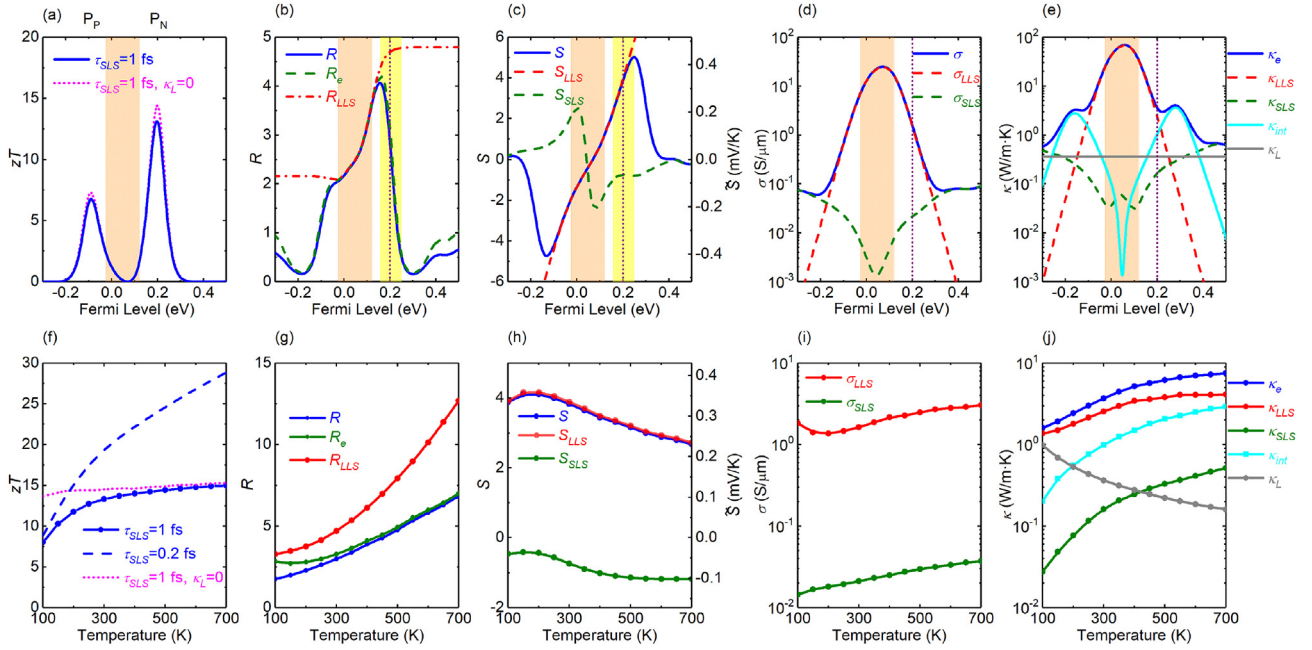


Fig. 2. TE transport properties of the single-layer ZrTe₅ ribbon. (a) Room-temperature figure of merit as a function of Fermi level with $\tau_{SLS} = 1$ fs and $\tau_{LLS} = 5$ ps. The TE parameters of the blue line is shown in (b-e). The lattice thermal conductivity κ_L (e) obtained from our *ab initio* calculations is used for calculating the blue line in (a). The magenta line in (a) has the same TE parameters as the blue line except that the lattice thermal conductivity κ_L is set as zero. P_P and P_N in (a) denote the zT peak energies respectively below and above the bulk gap (orange-shaded region). The latter is also denoted in (b-e) by vertical dotted lines. Yellow-shaded region in (b, c) shows the energy interval around P_N where the ratio R_e decreases with increasing Fermi level while the magnitude of the Seebeck coefficient increases. (f) Figure of merit at P_N as a function of temperature. The solid line is for $\tau_{SLS} = 1$ fs and its corresponding TE parameters are shown in (g-j). The blue dashed line in (f) is for $\tau_{SLS} = 0.2$ fs indicative of the highly defected case, and the magenta dotted line for $\kappa_L = 0$.

violated. **(III) Defect effect:** By properly introducing defects in the middle region of the ribbon, both the electronic and lattice thermal-conductivity are significantly reduced while the electrical conductivity is nearly unaffected. **(IV) Strain effect:** An appropriate strain further downsizes the bulk energy gap comparable to the thermal energy $k_B T$ and thus extremely violate the Wiedemann-Franz law, giving rise to a tens of times larger electrical to the electronic thermal conductivity ratio. These arresting features, particularly the anomalous Seebeck effect and the Wiedemann-Franz law violation, play the main roles to achieve the exceptionally high TE performance of $zT > 10$ much larger than $zT \sim 0.3$ of the bulk specimens [42], opening a route to the ultra-high TE efficiency.

2. Results and discussion

2.1. Electronic structures and electron scattering

The crystal structure of the single-layer ZrTe₅ in the x - z plane is shown in Fig. 1a. It is composed of alternate trigonal prismatic ZrTe₃ chains (yellow shaded) along the x direction and parallel zigzag Te chains stacking in the z direction. The geometrically optimized lattice constants are 4.05 Å and 13.86 Å in x and z directions, respectively. The single-layer ZrTe₅ is in the TI phase due to the band inversion around Γ , where the spin-orbit coupling opened energy gap E_g^{dir} as shown in Fig. 1c [37]. The direct band gap E_g^{dir} of 313 meV is much larger than the indirect full gap E_g^{indir} of 143 meV.

To further investigate TE properties of TI nanostructures, we consider the geometrically optimized ZrTe₅ ribbon extended along the x direction with a finite width of 14.1 nm (10 unit cells) along z direction as shown in Fig. 1b. The electronic structure is shown in Fig. 1d, in which the color of dots represents the atomic contributions from Te₂ (ZrTe₃) terminated half side indicated in Fig. 1b. For the topological edge states, more than 90% of the charge is localized within either the Te₂ half side (blue) or the ZrTe₃ half side (red), while, for the bulk states

(other colors), the charge mostly distributed in the middle bulk region. The corresponding bulk gap $E_g^{Ribbon} = 147$ meV (orange region) of ZrTe₅ ribbon is in good agreement with the full gap $E_g^{indir} = 143$ meV of the ZrTe₅ monolayer (yellow region in Fig. 1c).

As shown in Fig. 1d, two topologically protected linear edge states with different Fermi velocities lie exclusively in the bulk band gap. The difference in slopes of these one-dimensional TESs is due to the asymmetric edge structures, of which one side is terminated with ZrTe₃ trigonal prismatic chain while the other side with the Te zigzag chain (Fig. 1b). The charge profiles (Fig. 1b) of the inner (outer) TES (Fig. 1d) clearly show their localized nature around the Te₂ (ZrTe₃) edge. Both their decay lengths are less than 3 nm, which are much smaller than the ribbon width, giving rise to the non-overlapping wave functions at opposite edges. Such a small decay length results from the large gap E_g^{dir} opened by the spin-orbit coupling [43,44]. Moreover, the backward nonmagnetic scattering between the in-gap TESs at the same edge is forbidden due to the opposite spin polarization between its initial and final states as illustrated in Fig. 1e. Consequently the relaxation time of the in-gap TESs, hereafter referred to as long lifetime states (LLSs), should be much larger than that of the bulk states, hereafter called short lifetime states (SLSs).

To deal with multiple channel carriers, we adopt the dual relaxation time model, which is a generalization of the conventional constant relaxation time model as described in the Method section [25,40]. In principle, the LLS relaxation time τ_{LLS} of two-dimensional TI ribbons should be much larger than that of three-dimensional TI thin films because the latter (former) do (not) have allowable scattering processes with scattering angles in between 0° and 180°. It has been shown that the room-temperature LLS relaxation time in TI films can be as large as hundreds of femtoseconds [25]. Therefore, for TI ribbons, an LLS relaxation time of several picoseconds, which is orders of magnitude longer than that of SLSs, should be reasonable. In this work, the LLS relaxation time of 5 ps is used in most calculations while the dependence of zT on LLS relaxation time from 0.5 to 6 ps is also discussed. On

the other hand, the SLS relaxation time is typically of the order of 1–10 fs [45], and susceptible to defects. Therefore, by properly introducing defects, the SLS relaxation time comparable with or smaller than 1 fs should be achievable. If the defects are controlled in the bulk-like middle region of the ZrTe₅ ribbon where the TES carrier is absent (Fig. 1b), the SLS relaxation time can be significantly reduced without noticeably changing the LLS relaxation time. This can be experimentally realized through techniques such as nanoimprint/ion implantation or scanning tunneling microscope (see Supplementary Information S8 for detailed discussion) [46,47]. As will be discussed later, the dramatic difference in the relaxation time between LLSs and SLSs originates unusual TE behaviors and hence strongly improves the TE performance.

2.2. TES-induced unconventional thermoelectric transport

Fig. 2a shows the room-temperature zT as a function of Fermi level for the ZrTe₅ ribbon with $\tau_{SLS} = 1$ fs and $\tau_{LLS} = 5$ ps. Two significant zT peaks near the band edges can be clearly seen: The n -type peak P_N is 79 meV ($3.1 k_B T$) above the conduction band minimum (CBM); the p -type peak P_P is 64 meV ($2.4 k_B T$) below the valence band maximum (VBM). More importantly, a very large zT value around 10 can be attained. In addition, even if we reduce τ_{LLS} to 0.5 ps, comparable with that of TI films [25], the zT , as demonstrated in Supplementary Information S6, remains unprecedentedly high. Such an unprecedentedly high zT comes from the unconventional TE behaviors caused by the in-gap topological edge state (TES) carriers in the TI nanostructure. Fig. 2b shows the electrical to the electronic thermal conductivity ratios with the maximum value of approximately 4 around P_N , which is far higher than unity, the value expected by the Wiedemann-Franz law. Such a strong violation of the well-believed WF law originates from the unusual electrical conductivity and electronic thermal conductivity of the in-gap TESs (i.e., LLSs) as shown in Figs. 2d and 2e, respectively. On the other hand, Fig. 2c compares the total Seebeck coefficient with the contribution from the LLSs and SLSs. As expected, the SLSs (green dashed curve) show very typical (e.g. Ref. [48]) behaviors. In strong contrast, the LLSs, i.e., the in-gap TESs, show completely different behaviors (red curve), leading to the greatly enhanced Seebeck coefficient (blue curve) around P_N and P_P . These unconventional TE behaviors provide excellent opportunities to resolve the long-standing low- zT problem caused by the trade-off between TE properties. In the following two sections, we will elaborate two in-gap TES-induced unusual phenomena that achieve the high- zT in TI nanostructures: the anomalous Seebeck effect and the Wiedemann-Franz law violation. We will focus on the P_N and the n -type ZrTe₅. The behaviors for the P_P and the p -type case are similar.

2.3. Normal and anomalous Seebeck effect

Fig. 3 shows the schematic diagrams of normal and anomalous Seebeck effects. As demonstrated in the Method section, the reduced Seebeck coefficient, $S = \varepsilon_f - \langle \varepsilon \rangle$, is proportional to the difference between the Fermi level E_f and the dimensionless differential conductivity (DDC) ($-\frac{\partial f}{\partial \varepsilon} \Sigma$) average energy $\langle E \rangle$. It is normally much smaller than unity for metals (a) because their transport distribution function (TDF) Σ around E_f depends weakly on energy so that the DDC average energy is very close to E_f . On the other hand, the anomalous Seebeck effect (c) can be realized in TI nanostructures by utilizing the long-relaxation-time TESs with LLS carriers below the CBM (b). As illustrated in (c), because the scattering of the SLS carriers is much stronger than that of LLS carriers, it acts effectively as a carrier energy filter suppressing the carrier transport around E_f above the CBM. Thus the DDC average energy $\langle E \rangle$ drops considerably below the CBM, resulting in a large magnitude of the reduced Seebeck coefficient over a wide temperature range (d). As shown in Figs. 2c and 3d, the magnitude of the room-temperature reduced Seebeck coefficient, S , at P_N energy, can be as

large as 3.8 ($\tilde{S} = 0.33$ mV/K), which is larger than that of most good TE materials.

2.4. Wiedemann-Franz law and its violation

The Wiedemann-Franz law states that the ratio of the electrical conductivity to the electronic thermal conductivity

$$R_{WF} = \frac{3e^2}{\pi^2 k_B^2 T} \quad (1)$$

is a constant for a given temperature. It implies that both the charge current and the electronic heat current are guided by the same scattering mechanism. Nevertheless, the charge current and the electronic heat current are evidently different in nature. The electrical conductivity is caused by the charge current with each electron carrying an elementary charge. While the electronic thermal conductivity is due to the electronic heat current that can be achieved through the exchanges between carriers with different energies [49]. The amount of the heat transport is the energy difference between the two exchanged carriers. Therefore, suppressing the energy distribution of the conduction electrons in general will decrease κ_e and hence increase the ratio σ/κ_e . Thus toward low temperature, the energy distribution of the conduction electrons narrows down and the ratio σ/κ_e increases as expected by the Wiedemann-Franz law (eq. (1)).

To enhance the ratio σ/κ_e at a given temperature, the Wiedemann-Franz law must be violated. To gain further insight into the Wiedemann-Franz law violation, we rewrite the solution of the Boltzmann transport equation, eq. (6), as $R_e = C^{-1} \delta^{-1}$. Consequently the DDC ($-\frac{\partial f}{\partial \varepsilon} \Sigma$) variance $\delta = \langle \varepsilon^2 \rangle - \langle \varepsilon \rangle^2$ (eq. (7)), measuring the DDC broadening along the reduced energy $\varepsilon = E/k_B T$, is the only factor affecting the Wiedemann-Franz law. The Wiedemann-Franz law is valid only if the TDF (Σ) is weakly energy-dependent. In this case, the DDC profile is nearly the same as the Fermi window function as illustrated in Fig. 3e. Thus, the DDC variance δ is nearly equal to C^{-1} (~ 3.3) resulting in nearly unity R_e . In TI nanostructures, the DDC profile can be severely distorted by the large difference in the scattering intensity between the LLS and SLS carriers leading to significant violation of the Wiedemann-Franz law. If the DDC profile vanishes above the CBM, the DDC variance δ is reduced to unity causing about 3.3 times enhancement in the ratio R_e (see Supplementary Information S5 for detailed derivation). In practical situations, the DDC does not completely vanish above the CBM due to the finite contribution of the SLS carriers (Fig. 3f). This will broaden the DDC profile causing a reduction in the ratio R_e . If the SLS contribution is completely vanished, the ratio R_e approaches its upper limit $R_{LLS} = \sigma_{LLS}/\kappa_{LLS} R_{WF}$. As shown in Fig. 3h or 2g, the ratio R_e is considerably smaller than the ratio R_{LLS} at P_N energy. At $T = 100$ K, incorporating the SLS carriers will cause a reduction from the ideal value $R_{LLS} = 3.3$ to a practical value $R_e = 2.8$.

As the temperature increases, the reduced gap $\varepsilon_g = E_g^{Ribbon}/k_B T$ decreases. Considerable portion of the low energy tail of the Fermi window function extends to the energy region below the VBM. Hence the Wiedemann-Franz law is further violated due to this additional suppression in the DDC variance as illustrated in Fig. 3g. The resulting R_{LLS} (R_e) can be even larger than 10 (5.8) as $T > 600$ K (Fig. 3h). Moreover, R is nearly equal to R_e above room temperature indicating that the lattice thermal conductivity κ_L barely deteriorates the TE performance. This is mainly due to the nearly scattering-free TESs, which causes κ_e much larger than κ_L (Fig. 2j).

Here we note that the significant violation of the Wiedemann-Franz law was mostly found in few strongly correlated systems at cryogenic temperature [50]. In our work, the violation of the Wiedemann-Franz law, having nothing to do with the strong correlation, results from the extremely large difference in the relaxation time between the in-gap TESs and bulk states. This mechanism is not limited to the low temperature, and hence opens a new way toward the TE power generator operating efficiently over a wide temperature range above the room

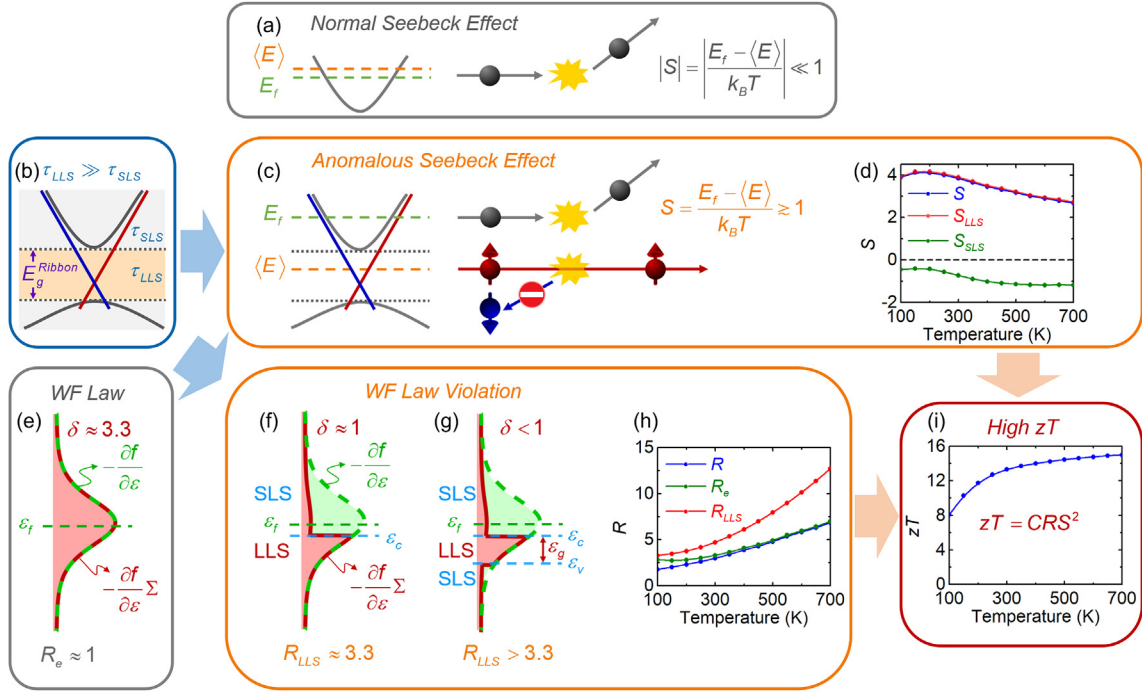


Fig. 3. Schematic diagram demonstrating the mechanisms of the high zT in TI nanostructures. The high zT is mainly due to the two unconventional phenomena: the anomalous Seebeck effect (c) and the Wiedemann-Franz (WF) law violation (f,g). Both are directly related to the large relaxation time difference between the LLSs and the SLSs (see text for details). For comparison, the normal Seebeck effect (a) and the WF law exhibited by common materials (e) are also included. (d,h,i) show the TE parameters of the single-layer ZrTe₅ ribbon for optimized n -type Fermi level (i.e., P_N energy) with $\tau_{SLS} = 1$ fs and $\tau_{LLS} = 5$ ps.

temperature. Combining the strong violation of the Wiedemann-Franz law here with the anomalous Seebeck effect discussed previously thus achieves extremely high figure of merit zT as shown in Fig. 3i over a wide temperature range.

2.5. Defect effect on the TE performance

As discussed previously, the high figure of merit results mainly from the dramatic difference between the SLS relaxation time τ_{SLS} and the LLS relaxation time τ_{LLS} . Therefore the TE performance can be further enhanced by reinforcing the difference between them. One simple way is to introduce defects into the middle bulk-like region of the TI ribbon by which τ_{SLS} can be significantly reduced without noticeably changing τ_{LLS} . Figs. 2f and S2a demonstrate that decreasing τ_{SLS} from 1 fs to 0.2 fs significantly improves the figure of merit. As shown in Figs. 2b–e ($\tau_{SLS} = 1$ fs) and Figs. S2b–S2e ($\tau_{SLS} = 1, 0.2$ fs), the LLS carriers dominate transport properties around the CBM no matter τ_{SLS} is 1 or 0.2 fs because τ_{LLS} is much larger than τ_{SLS} while the SLS carrier concentration is not yet overwhelming the LLS one. Thus, the figure of merit increases with increasing Fermi level due to the increases of both the R_{LLS} and the magnitude of the S_{LLS} . When the Fermi level further increases, the TE transport parameters deviate from their LLS counterpart causing the reduction in both the ratio R and the magnitude of the Seebeck coefficient. As shown in Figs. S2b and S2c, such reductions occur at a higher Fermi level for $\tau_{SLS} = 0.2$ fs (highly defected cases) than the undefected/less-defected case ($\tau_{SLS} = 1$ fs), leading to a higher zT for the highly defected case (Fig. S2a).

The electronic thermal conductivity κ_e has an additional component κ_{int} (Method section), which arises from the carrier inter-channel exchanges between the LLSs and the SLSs. Because of this additional term, the significant deviations of κ_e and R_e from their LLS contributions occur at a lower energy than those of σ and S . Therefore, the energy of the R_e peak is lower than that of the maximum magnitude of the Seebeck coefficient as shown in Figs. S2b and S2c. The P_N energy thus lies between these two peaks (yellow-shaded region in Figs. 2b and 2c

for $\tau_{SLS} = 1$ fs). The optimized zT and P_N are governed by the trade-off between the ratio R_e (R) and the Seebeck coefficient. This scenario of optimizing carrier concentration is very different from the typical one discussed in Introduction (or more detailedly in Ref. [15]) due to the qualitatively different behaviors of the TE parameters.

It is worth noting that the strong energy dependence of the TDF is generally expected in good TE systems. This is the fundamental reason why good TE materials typically are semiconductors, in which the dramatic variation of the density of states near the band edge originates the strong energy dependence of the TDF. Many efforts have been devoted to further strengthen the energy dependence of the TDF through various strategies such as low dimensional systems (e.g. quantum wells [21], quantum wires [22], and quantum dot superlattices [24]), conventional energy filters (e.g. superlattices [51], nanoparticles and grain boundaries [52,53]), ionized impurities [54], and resonant levels [55]. However, the carrier velocities are usually low in semiconductors owing to the near-band-edge nature. Introducing energy filters and/or impurities will intensify the carrier scattering and may degrade the TE performance. In contrast, for the TI nanoribbon proposed in this work, the electrical conductivity mostly comes from the in-gap TES (i.e., the LLS) carriers with high carrier velocities. The strongly energy-dependent TDF is driven by the drastic difference between the LLS and SLS relaxation times. As shown in Figs. 2d and 2i, increasing LLS relaxation time is beneficial to the electrical conductivity because the total conductivity σ is nearly equal to the LLS conductivity σ_{LLS} around the optimized Fermi level (i.e., P_N or P_p energy), whereas reducing SLS relaxation time does not change the electrical conductivity noticeably.

2.6. Further violation of Wiedemann-Franz law induced by strain

As discussed previously, the Wiedemann-Franz law violation with $R_e > 3.3$, $\delta < 1$ (Fig. 3g) can be achieved through reducing the reduced gap ϵ_g with increasing temperature. In fact, $\epsilon_g = E_g^{Ribbon}/k_B T$, at a given temperature, can be further reduced by applying strain. As demonstrated in Supplementary Information S1, either the uniaxial tensile or

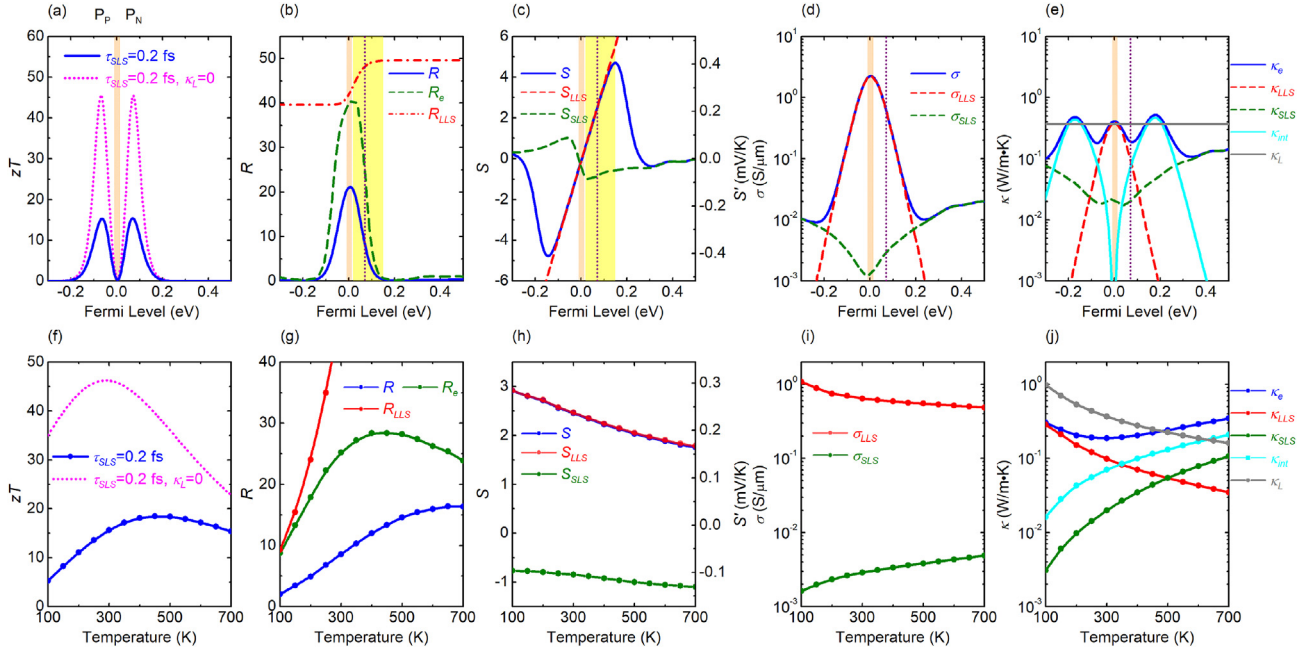


Fig. 4. TE transport properties of single-layer ZrTe₅ ribbon under a uniaxial tensile strain of 4% along the z direction with $\tau_{SLS} = 0.2$ fs indicative of the highly defected case and $\tau_{LLS} = 5$ ps. (a) Room-temperature figure of merit as a function of Fermi level. The TE parameters of the blue line is shown in (b–e). The lattice thermal conductivity κ_L (e) obtained from our *ab initio* calculations is used for calculating the blue line in (a). The magenta line in (a) has the same TE parameters as the blue line except that the lattice thermal conductivity κ_L is set as zero. P_P and P_N in (a) denote the zT peak energies respectively below and above the bulk gap (orange-shaded region). The latter is also denoted in (b–e) by vertical dotted lines. Yellow-shaded region in (b, c) shows the energy interval around P_N where the ratio R_e decreases with increasing Fermi level while the magnitude of the Seebeck coefficient increases. (f) Figure of merit at P_N as a function of temperature. The TE parameters of the blue line are shown in (g–j). The magenta dotted line in (f) is for $\kappa_L = 0$.

compressive strain along either the x or z direction can significantly reduce the ribbon bulk gap E_g^{Ribbon} . As an example, we consider the 4% tensile strain along the z direction leading to a small E_g^{Ribbon} of 22.8 meV (Fig. S1d) comparable with the room-temperature thermal energy and, correspondingly, a quite low reduced energy gap $\varepsilon_g = 0.88$. The resulting value of R_e , as shown in Fig. 4b, can be up to 40 extremely violating the Wiedemann-Franz law, $R_e \approx 1$.

Although the ratio R_e can be very high, the ratio R is significantly lower (Fig. 4g) indicating a small κ_e comparable or much smaller than κ_L (Fig. 4j). Such a small value of κ_e can be attributed to two phenomena caused by small E_g^{Ribbon} : 1. the small DDC variance δ and 2. the low LLS carrier concentration. The former is beneficial to the TE performance because it increases the R_{LLS} and hence the R_e . However, the latter is detrimental because it facilitates the deviation of the κ_e (R_e) from the κ_{LLS} (R_{LLS}). As shown in Fig. 4b, the room-temperature difference between the R_e and R_{LLS} is noticeable, even if the Fermi level lies in the LLS energy region. When the Fermi level is optimized at the P_N energy, the value of R_e is only about half of the R_{LLS} . Because the LLS-SLS exchange term, κ_{int} , is the main cause of the deviation of the κ_e from the κ_{LLS} (Figs. 2j and 4j), the reduction in the LLS carrier concentration will drive the P_N energy toward the LLS region causing the decrease in the magnitude of the Seebeck coefficient (cf. Figs. 4h and S3b). Consequently, the strained ribbon has a smaller zT than the unstrained ribbon (cf. Figs. 4f and S3a), even though its R_e is much larger (cf. Figs. 4g and S3c).

In this work, we also obtain the lattice thermal conductivity through *ab initio* calculations, in which we do not consider the reduction of the lattice thermal conductivity caused by defects. To see the effect of the κ_L reduction on the TE performance, we calculate the figure of merit in the extreme case of $\kappa_L = 0$ as indicated by the magenta dotted lines in Figs. 2a and 2f. For the unstrained case shown in Fig. 2a and f, the figure of merit with $\tau_{SLS} = 1$ fs is not sensitive to the reduction in the lattice thermal conductivity above room temperature because the lattice contribution κ_L is much smaller than the electronic contribution κ_e

as shown in Figs. 2e and 2j. Therefore it is unlikely to improve the TE performance by reducing the lattice thermal conductivity. On the other hand, because of the low electronic thermal conductivity discussed previously, the strained figure of merit with $\tau_{SLS} = 0.2$ fs can be largely enhanced by suppressing the lattice thermal conductivity as shown in Figs. 4a and 4f.

3. Conclusions

We systematically investigate the TE properties of single-layer topological insulator ZrTe₅ nanoribbons through the Boltzmann transport theory with electronic bands and lattice thermal conductivity obtained from *ab initio* calculations. We demonstrate that the dramatic difference in the relaxation time between the TESs and the 2D bulk states originates unconventional TE behaviors leading to extremely high TE performance as long as the Fermi level is properly tuned. A figure of merit larger than ten is viable mainly due to the strong Wiedemann-Franz law violation associated with the anomalous Seebeck effect. The calculated reduced Seebeck coefficient is much higher than unity and than that of most good TE materials as well. The widely accepted Wiedemann-Franz law is strongly violated with the ratio of the electrical conductivity to the electronic thermal conductivity several times greater than that expected by this law. By properly introducing defects in the middle 2D-bulk region of the ribbon, not only the lattice part but also the electronic part of the thermal conductivity can be significantly reduced without noticeably deteriorating the electrical conductivity, leading to further improvement in the TE performance. Under a suitably applied strain, the ratio R_e could even be raised up to tens of times violating the Wiedemann-Franz law. In addition, as demonstrated in the Supplementary Information S4, the single-layer topological insulator ZrTe₅ with a bulk gap smaller than 0.15 eV is almost exempted from the negative effects caused by the bipolar effects, which in general may seriously deteriorate the TE performance of normal small-gap semiconductors. These excellent TE behaviors give a new paradigm to

design high conversion efficiency TE devices.

4. Method

4.1. Electronic structure

The electronic structure is calculated through the projector augmented wave (PAW) approach within the framework of density functional theory as implemented in the Vienna *ab initio* Simulation Package (VASP) [56–58]. The exchange-correlation is described in the Perdew-Burke-Ernzerhof (PBE) form of generalized gradient approximation (GGA) [59,60]. The spin-orbit coupling is incorporated in the self-consistent calculations. The parameters used in the calculations, such as the cutoff of augmented plane waves and sampling of the Brillouin zone, are carefully checked to ensure the convergence. All the internal atomic coordinates and the lattice constant are relaxed until the magnitude of the force acting on all atoms is less than 0.001 eV/Å.

4.2. Electronic transport properties

The figure of merit zT can be expressed as

$$zT = CRS^2, \quad (2)$$

in which the C , R , and S are all dimensionless. The $C = 3/\pi^2$ is a constant, S the reduced Seebeck coefficient, $R = \sigma/\kappa R_{WF}$ the electrical-to thermal-conductivity ratio divided by $R_{WF} = Ce^2/k_B^2 T$, the value expected from the Wiedemann-Franz law [61], T the absolute temperature, k_B the Boltzmann constant, and e the elementary charge. The total thermal conductivity κ includes the electronic part κ_e and lattice part κ_L . In this work, the lattice thermal conductivity κ_L , as will be described in the ‘‘Phonon transport’’ subsection, is calculated through the harmonic and anharmonic interatomic force constants obtained from density functional perturbation theory. All the other TE parameters are calculated from the Boltzmann transport equation based on *ab initio* results, and can be expressed in terms of the dimensionless differential conductivity (DDC), i.e., the product of the dimensionless Fermi window function and the dimensionless transport distribution function (TDF) (Σ),

$$X = -\frac{\partial f}{\partial \varepsilon} \Sigma, \quad (3)$$

in which $f = (e^{\varepsilon - \varepsilon_f} + 1)^{-1}$ is the dimensionless Fermi Dirac distribution function, $\varepsilon = E/k_B T$ ($\varepsilon_f = E_f/k_B T$) the reduced energy (reduced Fermi level). The TDF Σ can be expressed as

$$\Sigma = \frac{\hbar}{2\pi a_B k_B T} \int d\mathbf{k} v_{\mathbf{k}}^2 \tau_{\mathbf{k}} \delta(\varepsilon - \varepsilon_{\mathbf{k}}), \quad (4)$$

in which $\varepsilon_{\mathbf{k}} = E_{\mathbf{k}}/k_B T$, $E_{\mathbf{k}}$ is the electronic band structure calculated through the density functional theory, $v_{\mathbf{k}}$ the group velocity, and $\tau_{\mathbf{k}}$ the relaxation time, \hbar the reduced Planck constant, and a_B the Bohr radius. The conductivity is proportional to the integral of the DDC,

$$\sigma = \sigma_0 \int d\varepsilon X, \quad (5)$$

in which $\sigma_0 = e^2 a_B / \hbar A$, and A is the ribbon cross section. The electronic thermal conductivity can be expressed as

$$\kappa_e = \frac{C\sigma\delta}{R_{WF}} = \left(\frac{k_B}{e}\right)^2 \sigma\delta T, \quad (6)$$

which is proportional to the variance of the DDC,

$$\delta = \langle \varepsilon^2 \rangle - \langle \varepsilon \rangle^2. \quad (7)$$

Here, the angle brackets, $\langle \xi \rangle \equiv \int d\varepsilon \xi X / \int d\varepsilon X$ is the average quantity ξ of the DDC. The DDC variance δ characterizes the spread of the DDC around the mean $\langle \varepsilon \rangle$. The reduced Seebeck coefficient is just the difference between the reduced Fermi level and the average reduced energy of the DDC, i.e.,

$$S = \varepsilon_f - \langle \varepsilon \rangle, \quad (8)$$

and the Seebeck coefficient is $\bar{S} = (k_B/e)S$.

4.3. Electronic transport properties based on dual relaxation time model

To calculate and analyze the transport properties caused by LLS and SLS channels, we adopt the dual relaxation time model, which is a generalization of the conventional constant relaxation time approximation [25,40]. In this model, the LLS and SLS relaxation times, τ_{LLS} and τ_{SLS} , are generally two different constants. The LLS (SLS) electrical conductivity σ_{LLS} (σ_{SLS}), the LLS (SLS) reduced Seebeck coefficient S_{LLS} (S_{SLS}), and the LLS (SLS) electronic thermal conductivity κ_{LLS} (κ_{SLS}) are the TE parameters contributed by merely the LLS (SLS) transport channel. They are calculated by equations of the same form as those of the previous section while only the LLSs (SLSs) are incorporated in the integrals. We can rewrite the TE parameters of the whole system in terms of these LLS and SLS TE parameters.

The electrical conductivity is just the sum of its LLS and SLS components,

$$\sigma = \sigma_{LLS} + \sigma_{SLS}. \quad (9)$$

The electronic thermal conductivity, unlike the case of the electrical conductivity, is not merely the sum of the LLS and the SLS contributions. It has an additional term κ_{int} , i.e.,

$$\kappa_e = \kappa_{LLS} + \kappa_{SLS} + \kappa_{int}, \quad (10)$$

in which

$$\kappa_{int} = \frac{k_B^2 T (S_{LLS} - S_{SLS})^2}{e^2 \sigma_{LLS}^{-1} + \sigma_{SLS}^{-1}} = \frac{k_B^2 T (\langle \varepsilon \rangle_{LLS} - \langle \varepsilon \rangle_{SLS})^2}{e^2 \sigma_{LLS}^{-1} + \sigma_{SLS}^{-1}}. \quad (11)$$

Here, the $\langle \varepsilon \rangle_{LLS}$ ($\langle \varepsilon \rangle_{SLS}$) is the average reduced energy of the DDC over the LLSs (SLSs). Given that the electronic thermal conductivity is defined under open circuit conditions, the heat transport brought by carriers can be achieved only through the exchanges of carriers with different energy [49]. The κ_{LLS} (κ_{SLS}) arises from the heat transport through the intra-channel exchanges between the LLS (SLS) carriers, while the κ_{int} through the inter-channel exchanges between the LLS and the SLS carriers. The reduced Seebeck coefficient is a conductance-weighted average of the those associated with the two types of carriers,

$$S = \frac{\sigma_{LLS} S_{LLS} + \sigma_{SLS} S_{SLS}}{\sigma_{LLS} + \sigma_{SLS}}. \quad (12)$$

4.4. Phonon transport

The lattice thermal conductivity is calculated through the almaBTE code with the harmonic and anharmonic (third-order) interatomic force constants (IFCs) as input [62]. Both the harmonic and the anharmonic IFCs are obtained through the *ab initio* calculations using the VASP as the computational engine [56–58]. The harmonic IFCs are calculated through the density functional perturbation theory [63], in which the $5 \times 1 \times 3$ supercell (180 atoms) with $3 \times 1 \times 3$ k -mesh is considered. The phonon dispersion is calculated by using the PHONOPY code with these harmonic IFCs as input [64]. As shown in Fig. S4a, the absence of imaginary frequencies in the phonon band structure guarantees the dynamical stability. In the calculation of the anharmonic IFCs, the THIRDORDER.PY script is used and the $5 \times 1 \times 3$ supercell (120 atoms) with $3 \times 1 \times 3$ k -mesh is considered [65]. The interactions up to the fifth-nearest neighbors are included. The phonon waves are assumed to be scattered specularly at the two ribbon edges. This gives the largest possible lattice thermal conductivity and hence would cause a conservative estimation of the TE performance. We also calculate lattice thermal conductivity under the diffusive boundary condition as functions of temperature. As shown in Fig. S4b, the reduction in the thermal conductivity caused by the diffusive boundary condition decreases with increasing temperature. At 100 K (700 K), the thermal conductivity

under diffusive boundary condition is 23% (7%) lower than that under specular boundary condition. The lattice thermal conductivity, as shown in Fig. 2j, decreases with increasing temperature. It is lower than 1 W/m²K above 100 K, and smaller than that of most known 2D materials [66].

Conflicts of interest

There are no conflicts of interest to declare.

Acknowledgement

This work was supported by the Ministry of Science and Technology, Taiwan. H.T.J. also thanks support from NCHC, CINC-NTU, iMATE-AS, and CQT-NTHU-MOE, Taiwan.

Appendix A. Supplementary data

Supplementary data to this article can be found online at <https://doi.org/10.1016/j.nanoen.2019.104092>.

References

- [1] D.M. Rowe (Ed.), CRC Handbook of Thermoelectrics, CRC Press, 1995.
- [2] T.M. Tritt, M.A. Subramanian, Thermoelectric materials, phenomena, and applications: a bird's eye view, *MRS Bull.* 31 (2006) 188–194.
- [3] G.J. Snyder, E.S. Toberer, Complex thermoelectric materials, *Nat. Mater.* 7 (2008) 105–114.
- [4] C.J. Vineis, A. Shakouri, A. Majumdar, M.G. Kanatzidis, Nanostructured thermoelectrics: big efficiency gains from small features, *Adv. Mater.* 22 (2010) 3970–3980.
- [5] J.F. Li, W.S. Liu, L.D. Zhao, M. Zhou, High-performance nanostructured thermoelectric materials, *NPG Asia Mater.* 2 (2010) 152–158.
- [6] T.M. Tritt, Thermoelectric phenomena, materials, and applications, *Annu. Rev. Mater. Res.* 41 (2011) 433–448.
- [7] H. Alam, S. Ramakrishna, A review on the enhancement of figure of merit from bulk to nano-thermoelectric materials, *Nano Energy* 2 (2013) 190–212.
- [8] W. He, G. Zhang, X.X. Zhang, J. Ji, G.Q. Li, X.D. Zhao, Recent development and application of thermoelectric generator and cooler, *Appl. Energy* 143 (2015) 1–25.
- [9] D.K. Aswal, R. Basu, A. Singh, Key issues in development of thermoelectric power generators: high figure-of-merit materials and their highly conducting interfaces with metallic interconnects, *Energy Convers. Manag.* 114 (2016) 50–67.
- [10] Q.H. Zhang, X.Y. Huang, S.Q. Bai, X. Shi, C. Uher, L.D. Chen, Thermoelectric devices for power generation: recent progress and future challenges, *Adv. Eng. Mater.* 18 (2016) 194–213.
- [11] X.L. Su, et al., Multi-scale microstructural thermoelectric materials: transport behavior, non-equilibrium preparation, and applications, *Adv. Mater.* 29 (2017) 1602013.
- [12] A. Ali, Y.X. Chen, V. Vasiraju, S. Vaddiraju, Nanowire-based thermoelectrics, *Nanotechnology* 28 (2017) 282001.
- [13] A.R.M. Siddique, S. Mahmud, B. Van Heyst, A review of the state of the science on wearable thermoelectric power generators (TEGs) and their existing challenges, *Renew. Sustain. Energy Rev.* 73 (2017) 730–744.
- [14] D. Champier, Thermoelectric generators: a review of applications, *Energy Convers. Manag.* 140 (2017) 167–181.
- [15] T.J. Zhu, et al., Compromise and synergy in high-efficiency thermoelectric materials, *Adv. Mater.* 29 (2017) 1605884.
- [16] J. He, T.M. Tritt, Advances in the thermoelectric materials research: looking back and moving forward, *Science* 357 (2017) 1369.
- [17] N. Xu, Y. Xu, J. Zhu, Topological insulators for thermoelectrics, *npj Quantum Materials* 2 (2017) 51.
- [18] D. Beretta, et al., Thermoelectrics: from history, a window to the future, *Mater. Sci. Eng. R* (2018), <https://doi.org/10.1016/j.mser.2018.1009.1000>.
- [19] K. Biswas, J.Q. He, I.D. Blum, C.I. Wu, T.P. Hogan, D.N. Seidman, V.P. Dravid, M.G. Kanatzidis, High-performance bulk thermoelectrics with all-scale hierarchical architectures, *Nature* 489 (2012) 414–418.
- [20] L.D. Zhao, V.P. Dravid, M.G. Kanatzidis, The panoscopic approach to high performance thermoelectrics, *Energy Environ. Sci.* 7 (2014) 251–268.
- [21] L.D. Hicks, M.S. Dresselhaus, Effect of quantum-well structures on the thermoelectric figure of merit, *Phys. Rev. B* 47 (1993) 12727–12731.
- [22] L.D. Hicks, M.S. Dresselhaus, Thermoelectric figure of merit of a one-dimensional conductor, *Phys. Rev. B* 47 (1993) 16631–16634.
- [23] G.D. Mahan, J.O. Sofo, The best thermoelectric, *Proc. Natl. Acad. Sci. U.S.A.* 93 (1996) 7436–7439.
- [24] T.E. Humphrey, H. Linke, Reversible thermoelectric nanomaterials, *Phys. Rev. Lett.* 94 (2005) 096601.
- [25] T.-H. Wang, H.-T. Jeng, Strongly enhanced thermoelectric performance over a wide temperature range in topological insulator thin films, *ACS Appl. Energy Mater.* 1 (2018) 5646–5655.
- [26] L. Fu, Hexagonal warping effects in the surface states of the topological insulator Bi₂Te₃, *Phys. Rev. Lett.* 103 (2009) 266801.
- [27] W.C. Lee, C.J. Wu, D.P. Arovas, S.C. Zhang, Quasiparticle interference on the surface of the topological insulator Bi₂Te₃, *Phys. Rev. B* 80 (2009) 245439.
- [28] X.T. Zhou, C. Fang, W.F. Tsai, J.P. Hu, Theory of quasiparticle scattering in a two-dimensional system of helical Dirac fermions: surface band structure of a three-dimensional topological insulator, *Phys. Rev. B* 80 (2009) 245317.
- [29] P. Roushan, et al., Topological surface states protected from backscattering by chiral spin texture, *Nature* 460 (2009) 1106–1109.
- [30] T. Zhang, et al., Experimental demonstration of topological surface states protected by time-reversal symmetry, *Phys. Rev. Lett.* 103 (2009) 266803.
- [31] Z. Alpichshev, et al., STM imaging of electronic waves on the surface of Bi₂Te₃: topologically protected surface states and hexagonal warping effects, *Phys. Rev. Lett.* 104 (2010) 016401.
- [32] I.K. Drozdov, et al., One-dimensional topological edge states of bismuth bilayers, *Nat. Phys.* 10 (2014) 664–669.
- [33] A.A. Taskin, S. Sasaki, K. Segawa, Y. Ando, Manifestation of topological protection in transport properties of epitaxial Bi₂Se₃ thin films, *Phys. Rev. Lett.* 109 (2012) 066803.
- [34] S.Y. Matsushita, et al., Thermoelectric properties of 3D topological insulator: direct observation of topological surface and its gap opened states, *Phys. Rev. Mater.* 1 (2017) 054202.
- [35] T.C. Hsiung, C.Y. Mou, T.K. Lee, Y.Y. Chen, Surface-dominated transport and enhanced thermoelectric figure of merit in topological insulator Bi_{1.5}Sb_{0.5}Te_{1.7}Se_{1.3}, *Nanoscale* 7 (2015) 518–523.
- [36] W. Liu, et al., Origins of enhanced thermoelectric power factor in topologically insulating Bi_{0.64}Sb_{1.36}Te₃ thin films, *Appl. Phys. Lett.* 108 (2016) 043902.
- [37] H.M. Weng, X. Dai, Z. Fang, Transition-metal pentatelluride ZrTe₅ and HfTe₅: a paradigm for large-gap quantum spin Hall insulators, *Phys. Rev. X* 4 (2014) 11002.
- [38] R. Wu, et al., Evidence for topological edge states in a large energy gap near the step edges on the surface of ZrTe₅, *Phys. Rev. X* 6 (2016) 021017.
- [39] X.B. Li, et al., Experimental observation of topological edge states at the surface step edge of the topological insulator ZrTe₅, *Phys. Rev. Lett.* 116 (2016) 176803.
- [40] Y. Xu, Z.X. Gan, S.C. Zhang, Enhanced thermoelectric performance and anomalous Seebeck effects in topological insulators, *Phys. Rev. Lett.* 112 (2014) 226801.
- [41] J.S. Zhang, et al., Disentangling the magnetoelectric and thermoelectric transport in topological insulator thin films, *Phys. Rev. B* 91 (2015) 075431.
- [42] S.A. Miller, et al., Polycrystalline ZrTe₅ parametrized as a narrow-band-gap semiconductor for thermoelectric performance, *Phys. Rev. Appl.* 9 (2018) 014025.
- [43] B.A. Bernevig, T.L. Hughes, S.C. Zhang, Quantum spin Hall effect and topological phase transition in HgTe quantum wells, *Science* 314 (2006) 1757–1761.
- [44] X.L. Qi, S.C. Zhang, Topological insulators and superconductors, *Rev. Mod. Phys.* 83 (2011) 1507.
- [45] F. Ricci, et al., Data descriptor: an *ab initio* electronic transport database for inorganic materials, *Sci. Data* 4 (2017) 170085.
- [46] W.-D. Li, W. Wu, R.S. Williams, Combined helium ion beam and nanoimprint lithography attains 4 nm half-pitch dense patterns, *J. Vac. Sci. Technol. B* 30 (2012) 06F304.
- [47] R.J. Celotta, et al., Invited article: autonomous assembly of atomically perfect nanostructures using a scanning tunneling microscope, *Rev. Sci. Instrum.* 85 (2014).
- [48] F.Q. Wang, S.H. Zhang, J.B. Yu, Q. Wang, Thermoelectric properties of single-layered SnSe sheet, *Nanoscale* 7 (2015) 15962–15970.
- [49] S. Datta, Lessons from Nanoelectronics: A New Perspective on Transport, World Scientific Publishing Company, 2012.
- [50] S. Lee, et al., Anomalously low electronic thermal conductivity in metallic vanadium dioxide, *Science* 355 (2017) 371.
- [51] A. Shakouri, J.E. Bowers, Heterostructure integrated thermionic coolers, *Appl. Phys. Lett.* 71 (1997) 1234–1236.
- [52] S.V. Faleev, F. Leonard, Theory of enhancement of thermoelectric properties of materials with nano-inclusions, *Phys. Rev. B* 77 (2008).
- [53] J.P.A. Makongo, et al., Simultaneous large enhancements in thermopower and electrical conductivity of bulk nanostructured half-Heusler alloys, *J. Am. Chem. Soc.* 133 (2011) 18843–18852.
- [54] S.Y. Wang, et al., On intensifying carrier impurity scattering to enhance thermoelectric performance in Cr-doped Ce₃Co₄Sb₁₂, *Adv. Funct. Mater.* (2015) 6660–6670.
- [55] J.P. Heremans, B. Wientlocha, A.M. Chamoire, Resonant levels in bulk thermoelectric semiconductors, *Energy Environ. Sci.* 5 (2012) 5510–5530.
- [56] G. Kresse, J. Furthmüller, Efficiency of *ab-initio* total energy calculations for metals and semiconductors using a plane-wave basis set, *Comput. Mater. Sci.* 6 (1996) 15–50.
- [57] G. Kresse, *Ab initio* molecular dynamics for liquid-metals, *J. Non-Cryst. Solids* 193 (1995) 222–229.
- [58] G. Kresse, J. Furthmüller, Efficient iterative schemes for *ab initio* total-energy calculations using a plane-wave basis set, *Phys. Rev. B* 54 (1996) 11169–11186.
- [59] J.P. Perdew, et al., Atoms, molecules, solids, and surfaces: applications of the generalized gradient approximation for exchange and correlation, *Phys. Rev. B* 46 (1992) 6671–6687.
- [60] J.P. Perdew, Y. Wang, Pair-distribution function and its coupling-constant average for the spin-polarized electron-gas, *Phys. Rev. B* 46 (1992) 12947–12954.
- [61] N.W. Ashcroft, N.D. Mermin, *Solid State Physics*, Holt-Saunders, 1976.
- [62] J. Carrete, et al., almaBTE: a solver of the space-time dependent Boltzmann transport equation for phonons in structured materials, *Comput. Phys. Commun.* 220 (2017) 351–362.
- [63] S. Baroni, S. de Gironcoli, A. Dal Corso, P. Giannozzi, Phonons and related crystal properties from density-functional perturbation theory, *Rev. Mod. Phys.* 73 (2001) 515–562.
- [64] A. Togo, I. Tanaka, First principles phonon calculations in materials science, *Scr. Mater.* 108 (2015) 1–5.
- [65] W. Li, J. Carrete, N.A. Katcho, N. Mingo, ShengBTE: a solver of the Boltzmann transport equation for phonons, *Comput. Phys. Commun.* 185 (2014) 1747–1758.
- [66] X.K. Gu, Y.J. Wei, X.B. Yin, B.W. Li, R.G. Yang, Colloquium: phononic thermal properties of two-dimensional materials, *Rev. Mod. Phys.* 90 (2018) 041002.